Ceramics International 52 (2026) 38721–38732

Contents lists available at ScienceDirect

Ceramics International

journal homepage: www.elsevier.com/locate/ceramint

Tuning structural, magnetic and electrical performance of Ni–Co ferrite/GNP composites via rare-earth doping for energy storage applications

Sana Riasat [a], Zeshan Munir [a,*], Maria Akhtar [a,b], Le Duc Tung [c,d], Rawiyah Alkahtani [e], Ohud Alzaidi [f], M.S. Al-Buriahi [g], Salah Knani [h,**], Shahir Hussain [i], Nguyen Thi Kim Thanh [c,d], Muhammad Imran Arshad [a,***]

[a] Magnetic & Innovative Materials in Nanotechnology (MIMI NanoTech) Research Lab, Department of Physics, Government College University, Faisalabad, Punjab, 38000, Pakistan
[b] Center for High Energy Physics, University of the Punjab, Lahore, Pakistan
[c] Biophysics Group, Department of Physics and Astronomy, University College London, Gower Street, London, WC1E 6BT, UK
[d] UCL Healthcare Biomagnetics and Nanomaterial Laboratories, 21 Albemarle Street, London, W1S 4BS, UK
[e] Department of Chemistry, College of Science, Princess Nourah bint Abdulrahman University, P.O. Box 84428, Riyadh, 11671, Saudi Arabia
[f] Department of Chemistry, College of Science - Al Khurma, Taif University, P.O. Box 11099, Taif, 21944, Saudi Arabia
[g] Department of Physics, Sakarya University, Sakarya, Turkey
[h] Center for Scientific Research and Entrepreneurship, Northern Border University, Arar, 73213, Saudi Arabia
[i] Department of Electrical and Electronic Engineering, College of Engineering and Computer Science, Jazan University, PO Box. 706, Jazan, 45142, Saudi Arabia

ARTICLE INFO

Keywords:
GNP composites
Ferrite-based composites
Sol-gel auto-combustion
Electrode material

ABSTRACT

In this research, we synthesized rare-earth element-doped Ni-Co ferrites graphene nanocomposites ($Ni_{0.2}Co_{0.8}RE_{0.06}Fe_{1.94}O_4$/3 wt% GNPs RE = Nd, Er, Pr, Lu, Ho) to study their structural, magnetic, electrical and dielectric properties. The XRD patterns confirm FCC spinel structure. The average crystallite sizes of the rare earth-doped samples ranged from 30.4 nm to 34.4 nm. SEM analysis confirms the successful synthesis of a nanostructured, porous ferrite-GNP composite with uniformly distributed grains and morphology well-suited for multifunctional applications. The magnetic analysis confirms the soft magnetic nature of synthesized composites due to moderate saturation magnetization ranged from 108.9 emu/g to 123.9 emu/g and coercivity ranged from 475.48 Oe to 835.12 Oe. The DC resistivity at room temperature ranged from 3.02×10^7 - 3.44×10^9 Ω cm at room temperature. The DC resistivity decreases with the rise in temperature, at 773 K it ranges from 1.53×10^4 Ω cm to 9.39×10^4 Ω cm. The dielectric characteristics, such as the dielectric constant (ε'), dielectric tangent loss ($\tan\delta$), AC conductivity and quality factor showed a strong frequency dependent behavior. The enhanced structural, electrical magnetic and dielectric properties of synthesized nanocomposites render them exceptionally promising as an electrode material in energy storage and other advanced technological fields.

1. Introduction

Nanocomposites of graphene nanoplatelets (GNPs) have emerged as multifunctional systems exhibiting enhanced mechanical integrity, high surface to volume ratio, improved electrical resistivity, and suitable thermoelectric responses [1,2]. These characteristics can also be controlled by chemical composition, synthesis conditions, and sintering temperature [3]. The general formula for spinel structure is AB_2O_4, here cations occupy tetrahedral (A) and octahedral (B) voids [4]. Recent researchers focused on combining ferrites with carbon or other materials which have excellent electronic properties, to form hybrid nanocomposites with synergistic performance [5,6]. The polymer based composites with ferrites also exhibit excellent properties for high frequency applications [7]. But carbon based composites have more excellent performance due to its conducting nature. Such GNPs based materials have large surface area, which facilitates electron

* Corresponding author.
** Corresponding author.
*** Corresponding author.
E-mail addresses: zeshan.202100059@gcuf.edu.pk, zeshanmunir8@gmail.com (Z. Munir), saleh.kenani@nbu.edu.sa (S. Knani), mimranarshad@gcuf.edu.pk, miarshad15@gmail.com (M.I. Arshad).

https://doi.org/10.1016/j.ceramint.2026.06.328
Received 28 April 2026; Received in revised form 11 June 2026; Accepted 21 June 2026
Available online 22 June 2026
0272-8842/© 2026 Elsevier Ltd and Techna Group S.r.l. All rights are reserved, including those for text and data mining, AI training, and similar technologies.

transportation [8,9]. Addition of GNPs with two or more metallic cations has proven to be an effective for tuning electrical, magnetic, and energy storage applications [10,11]. When ferrites combined with GNPs, such doped ferrites yield composites with enhanced space charge effect, electrochemical and electro-thermal behavior, beneficial for stealth and energy-related technologies [12–14]. The extended surface area of GNPs also support in transportation of charges and interfacial coupling [15,16]. There are several methods to synthesize spinel ferrites like hydrothermal [17], co-precipitation [18] and sol gel auto combustion [19].

In particular, nickel–cobalt ferrite ($NiCoFe_2O_4$) – often with an equal ratio of Ni:Co, shows high structural symmetry with relatively low magneto-crystalline anisotropy [20]. These soft ferrites have improved structural, dielectric and magnetic properties that supports their use in advanced technologies such as sensors, microwave devices, supercapacitors, and even biomedical applications [21,22]. Spinel ferrites have high losses as compare to hexa ferrites [23]. But these losses are reduced due to addition of GNPs and suitable for microwave devices [24]. Due to tunable magnetic, chemical and functional characteristics, spinel ferrites are favorable candidate for biomedical applications [25]. The magnetic softness of ferrites also influenced by the replacement of A site and B site cations as reported hexa ferrites, $Sr_{1-x}Mn_xFe_{12-x}Y_xO_{19}$ (with $0.0 \leq x \leq 0.5$) revealed that the magnetic interactions were weakened with the replacement of both Sr^{2+} and Fe^{3+} ions by the Mn^{2+} and Y^{3+} dopants [26].

Substituting a small fraction of the Fe^{3+} cations with trivalent rare-earth ions (e.g. Nd^{3+}, Pr^{3+}, Er^{3+}, Lu^{3+}, Ho^{3+}) provides another powerful way to tailor ferrite properties [27,28]. Rare-earth ions (RE) have much larger ionic radii than Fe^{3+}, so their incorporation strains the spinel lattice and modifies cation distributions. Even modest RE doping can markedly change a ferrite's dielectric and magnetic behavior. For example, lanthanum, gadolinium or neodymium substitution in $CoFe_2O_4$ spinels has been reported to reduce the static dielectric constant with higher RE content [29,30]. Similarly, Nd^{3+} substitution in Co ferrite sharply increased its coercivity while lowering dielectric loss. In Ni and Co spinel's alike, RE doping often decreases saturation magnetization because most RE^{3+} (unlike Fe^{3+} with 5 μ_B) contribute only weak paramagnetic moments. Indeed, in Gd^{3+}-doped $Ni_{0.5}Co_{0.5}Fe_2O_4$ nano-crystals, the saturation magnetization falls significantly (e.g. from ≈29.8 to 20.8 emu/g as Gd-content rises) while coercivity more than doubles [31]. This decline in magnetization is attributed to the replacement of magnetic Fe^{3+} ions (in octahedral sites) with largely paramagnetic Gd^{3+} [28]. Vibrating-sample magnetometer (VSM) studies on Pr^{3+}-doped Ni–Co ferrite similarly show that M_s and M_r decrease while the coercive field H_c increases with higher Pr^{3+} content. The overall effect of RE substitution depends on the ion's 4f configuration: for example, Ho^{3+} and Er^{3+} (with high 4f moments of ~10 μ_B and 9.6 μ_B) might boost magnetization differently than non-magnetic Lu^{3+} ($4f^{14}$, 0 μ_B) or moderately magnetic Nd^{3+} (3.3 μ_B) [29]. In general, introducing RE ions tends to deform the spinel structure, change the lattice constant (often expanding it), and shift magnetic anisotropies. The altered cation distribution and exchange pathways also impact dielectric relaxation and conductivity: space-charge polarization at grain boundaries is modified [12]. For instance, La^{3+}-substitution in Co–Zn ferrite lowered M_s to drop (from 55.8 to 22.1 emu/g) while raising H_c [31]. Ni-Zn ($Ni_{0.4}Zn_{0.6}Fe_2O_4$) spinel ferrites have been reported with a saturation magnetization of 74.6 emu/g [32].

Nickel–cobalt ferrite in particular has been previously doped with various RE elements, often forming single-phase spinel phases [33]. For example, $Ni_{0.5}Co_{0.5}Fe_{1.97}Nd_{0.03}O_4$ was synthesized as a single-phase cubic spinel, and similarly $Ni_{0.5}Co_{0.5}Fe_2O_4$ doped with Gd^{3+} or Pr^{3+} remains a homogeneous spinel with gradually changing lattice parameters. In all cases, small amounts of heavy RE in the B-site typically reduce M_s and shift the magnetic behavior toward higher coercivity or even super paramagnetic [34]. These modifications are coupled with measurable changes in electrical transport: RE doping tends to narrow the band gap or introduce mid-gap states, and it can increase the permittivity at low frequencies. In summary, doping Ni–Co ferrite with Nd, Er, Pr, Lu or Ho is expected to distort the lattice, reduce net ferrimagnetism (by diluting Fe^{3+}–Fe^{3+} exchange), and tailor the dielectric properties [15,35].

In this work, we synthesize $Ni_{0.2}Co_{0.8}Fe_2O_4$/3 wt% GNPs (NCF) and its rare-earth-doped derivatives $Ni_{0.2}Co_{0.8}RE_{0.06}Fe_{1.94}O_4$/3 wt% GNPs [RE = Nd (NCNdF), Er (NCErF), Pr (NCPrF), Lu (NCLuF), Ho (NCHoF)] and incorporate them with graphene nanoplatelets to form multifunctional nanocomposites. The crystal structure and phase purity are confirmed by X-ray diffraction (XRD), with expected cubic spinel patterns and lattice parameter shifts indicating RE substitution. Scanning electron microscopy (SEM) was used to examine surface morphology and it confirms GNPs sheets are well-interfaced with ferrite particles. Magnetic properties are measured via vibrating-sample magnetometer (Model VSM-175) to evaluate saturation magnetization (M_s), coercivity (H_c), and magnetic anisotropy changes due to doping and composite formation. Finally, DC electrical resistivity was measured to quantify how GNPs and RE doping jointly influence charge transport, bridging the ferrite (normally an insulator) to a more conductive composite. By correlating these structural, magnetic, electrical and dielectric, we aim to demonstrate how rare-earth substitution and graphene inclusion together tailor the structural, morphological, magnetic and resistive characteristics of Ni–Co ferrites nanocomposites, opening routes to optimized materials for next-generation electrodes and energy storage applications.

2. Materials synthesis and methodology

2.1. Synthesis procedure

In this research, we employed highly pure analytical reagents to synthesize $Ni_{0.2}Co_{0.8}RE_{0.06}Fe_{1.94}O_4$ spinel ferrite composites doped with graphene nanoplatelets (GNPs) through the sol-gel auto-combustion process. The reagents used included nickel(II) nitrate trihydrate [$Ni(NO_3)_2{\cdot}3H_2O$], cobalt(II) nitrate hexahydrate [$Co(NO_3)_2{\cdot}6H_2O$], iron (III) nitrate nona-hydrate [$Fe(NO_3)_3{\cdot}9H_2O$], rare-earth element nitrates (RE = Nd, Er, Pr, Lu, Ho), citric acid monohydrate [$C_6H_8O_7{\cdot}H_2O$], and graphene nanoplatelets (GNPs). The initial step in the synthesis involved dissolving the metal nitrates in a precise quantity of distilled water. This solution was stirred continuously to ensure homogeneity, resulting in the formation of a sol. Citric acid was used as a fuel agent, in a 1:2 M ratio with the metal nitrates. Ammonia (NH_3) solution was added dropwise to adjust the pH to approximately 7. After maintaining the pH, the heat was turned on, and the solution was stirred continuously. The sol transformed slowly into a gel and then into fluffy ashes after burning. Those fluffy ashes were ground and sintered at 973 K for 5 h to enhance crystallinity and phase formation. After sintering, sintered samples were again grounded to obtain homogeneous powder which was used for characterizations. The complete synthesis is described in Fig. 1.

2.2. Characterizations techniques

We employed various techniques to characterize the materials. The D8 Advance XRD model (Bruker, Germany) was used to study X-ray diffraction (XRD) patterns, while the SEM Cubes 10 (Emcraft, South Korea) and JEM-1010 transmission electron microscope (JEOL, Japan) were used to examine the surface morphology. We employed a VSM-175 vibrating sample magnetometer (Dexinmag, China) instrument, to measure magnetic properties. We employed a two-point probe technique with a source meter, Keithley 2401 (Keithley Instruments, USA) to determine the DC electrical resistivity and utilized an LCR meter HIOKI IM-3536 LCR meter (HIOKI E.E. Corporation, Japan) to examine the dielectric properties.

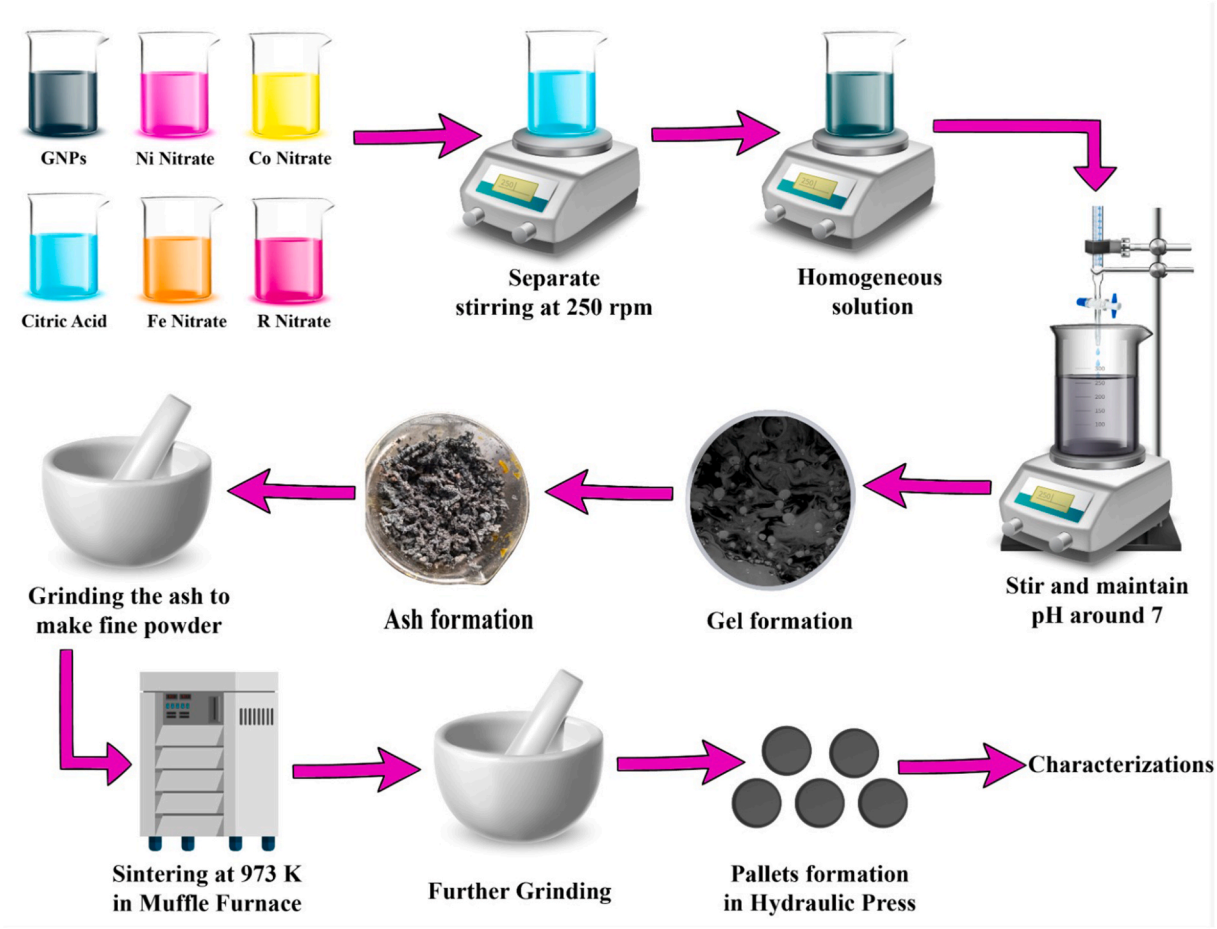


Fig. 1. Schematic diagram of synthesis of samples by sol-gel technique.

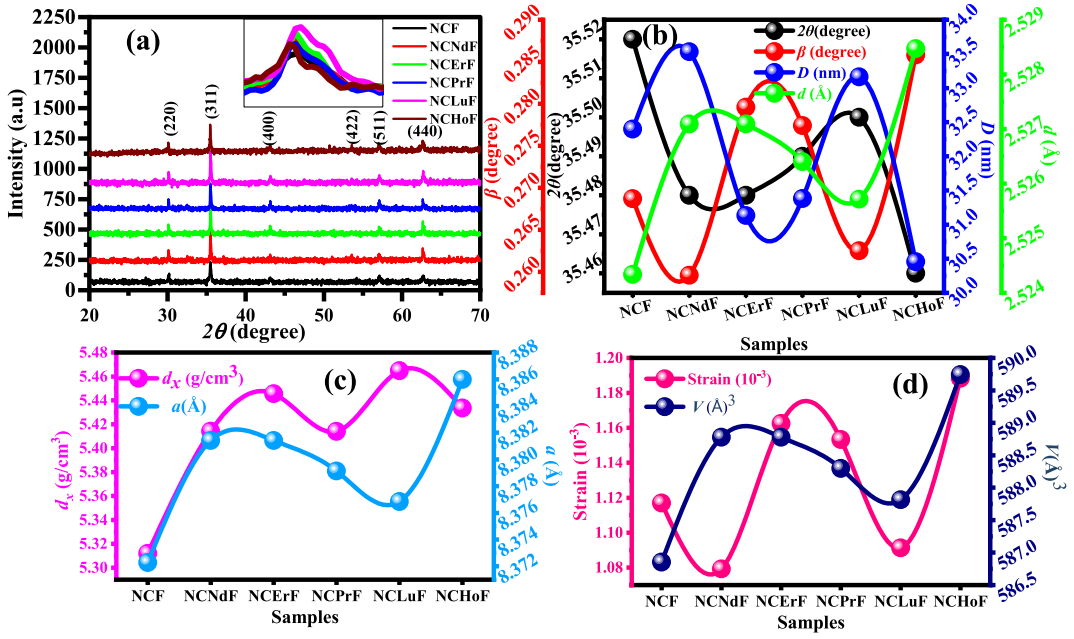


Fig. 2. (a) XRD spectra (inset (311) peak shift), (b) 2θ, β, D and d-spacing (c) d_x and lattice constant a, and (d) Strain and unit cell volume vs samples of $Ni_{0.2}Co_{0.8}RE_{0.06}Fe_{1.94}O_4$/3 wt% GNP composites.

3. Result and discussion

3.1. Structural analysis by XRD

The structural properties of $Ni_{0.2}Co_{0.8}Fe_2O_4$/GNPs and rare earth (RE)-doped $Ni_{0.2}Co_{0.8}RE_{0.06}Fe_{1.94}O_4$/GNP nanocomposites were investigated through X-ray diffraction (XRD) analysis. The synthesized samples were thermally treated at 973 K for 5 h to enhance crystallinity. The XRD spectra confirmed the presence of a single-phase cubic spinel structure corresponding to Ni–Co ferrite/GNPs composites. No extra peak for secondary phase is observed in the XRD data, which also confirms the oxygen stoichiometry in the synthesized composites. The prominent diffraction peaks were observed at 2θ values of 30.04°, 35.61°, 43.25°, 56.96°, and 62.76°, which were indexed to the (220), (311), (400), (511), and (440) crystallographic planes, respectively, as shown in Fig. 2 [36]. Among these, the (311) reflection exhibited the highest intensity and appeared within 35.46° to 35.52°, indicating it as the most dominant peak. The crystallite sizes were computed using the Debye–Scherrer equation:

$$\text{Crystallite size } (D) = \frac{k\lambda}{\beta \cos\theta} \quad (1)$$

Here, K is Scherrer constant (typically 0.9), λ is the wavelength of incident X-rays, β is the full-width at half-maximum (*FWHM*), and θ is the Braggs angle [37]. The incorporation of GNPs into the spinel lattice introduced structural distortion, as evidenced by a shift in the (311) peak position toward lower 2θ values as depicted in inset Fig. 2 (a). This shift was more pronounced with the substitution of rare earth ions into the spinel framework, indicating lattice strain and site distortion due to ionic radius mismatch. Moreover, the presence of rare earth dopants led to an increase in interplanar spacing (d-spacing), as detailed in Table 1 and Fig. 2(b). No secondary phases or impurities were detected, confirming the phase purity and high crystallinity of the synthesized materials [10]. A broad reflection attributed to the GNPs phase was observed, which may result from its inherently low crystallinity. Differences in XRD peak intensities among the samples were attributed to variations in cation distribution, local distortions, and changes in shared/unshared edge geometries within the spinel structure. The average crystallite sizes of the rare earth-doped samples ranged from 34.37 nm to 30.43 nm, depicted in Fig. 2 (b). These variations are attributed to the ionic size of the dopant cations, where larger radii induced more significant lattice expansion compared to smaller ions [27]. The d-spacing, X-ray density, lattice constant, strain and unit cell volume ranged from 2.5243 Å to 2.5284 Å, 5.3119 g/cm^3 to 5.4649 g/cm^3, 8.3722 Å to 8.3859 Å, 1.08 to 1.19 and 586.85 Å^3 to 589.74 Å^3 respectively as described in Table 1 and Fig. 2(c) and (d). Among all the synthesized composites, the NCPrF sample was found to be the most promising candidate as electrode material because of its optimized structural parameters, optimized crystallite size value of 31.36 nm, intermediate lattice constant and unit cell volume, showing the least lattice distortion.

The Rietveld refinement of XRD patterns of synthesized composites are shown in Fig. 3(a–f). The refinement of all the patterns of synthesized composites was based on cubic spinel structure with *Fd-3m* space group. The observed peaks correspond to the spinel phase. The calculate R-factors (R_{wp}, R_{exp}, and χ^2) are presented in Table 1, their values are in an acceptable range and confirm the reliability of spinel structure of all synthesized samples [38,39]. The calculated site occupancy (g), atomic positions ($x = y = z$) and cationic distributions are presented in Table 2. The doped rare earth elements occupy B-sites, the size of B-sites is greater than A-sites because of large ionic radius of rare earth elements as shown in Fig. 4.

3.2. Scanning electron microscopy (SEM)

The morphological characteristics of the synthesized rare-earth-doped $Ni_{0.2}Co_{0.8}Fe_{1.94}O_4$/graphene nanocomposites were investigated using scanning electron microscopy (SEM), as presented in Fig. 5. The SEM micrograph exhibits a microstructure comprising densely packed nano-sized grains with a relatively uniform distribution [40]. Upon closer examination, the particles demonstrate a quasi-spherical to polyhedral shape with visible inter-particle voids. These voids and porous regions are likely a result of the liberation of gaseous by-products during the combustion of citric acid in the sol-gel auto-combustion synthesis route, which make them suitable as electrode material for energy storage devices [41–43]. Such morphological porosity is considered beneficial for applications requiring high surface area, such as electrochemical energy storage, photocatalysis, and adsorption-based separation technologies [10,20].

Notably, the incorporated GNPs layers in composites are not distinctly visible because of the low weight percentage and their extremely thin layers; however, their presence can be inferred from the decline in agglomeration of ferrite particles [44]. The GNP matrix likely gives a conductive support to the ferrite nanoparticles, enhancing charge transportation and conductivity of the synthesized composites [45,46]. Moreover, the interfaces between the ferrite particles and the GNPs sheets appear coherent, in the form of agglomerates [42,47]. The interface between GNPs and ferrite particles improves conductivity, mechanical strength, and charge transport like properties [43,46]. The compactness and grain connectivity in the microstructure also suggest efficient densification, which is desirable for enhancing magnetic, electrical, and electrochemical performance [20,48,49]. In conclusion, the SEM analysis confirms the successful synthesis of a nanostructured, porous ferrite-graphene composite with uniformly distributed grains and a morphology well-suited for multifunctional applications [50]. The observed features reflect the influence of rare earth elements doping and GNP integration on the morphological evolution of the material during thermal processing [42,51].

Table 1
XRD parameters of $Ni_{0.2}Co_{0.8}RE_{0.06}Fe_{1.94}O_4$/3 wt% GNP composites.

Sample ID	2θ (degree)	β (degree)	*hkl*	D (nm)	d (Å)	d_x (g/cm^3)	a (Å)	ε (10^{-3})	V (Å)^3	R_{wp}	R_{exp}	χ^2
NCF	35.52	0.2687	(311)	34.37	2.524	5.3119	8.3722	1.12	586.85	73.10	56.50	1.29
NCNdF	35.48	0.2596	(311)	33.50	2.527	5.4142	8.3814	1.08	588.77	65.66	45.38	1.45
NCErF	35.48	0.2796	(311)	31.11	2.527	5.4455	8.3814	1.16	588.77	82.35	55.86	1.47
NCPrF	35.49	0.2774	(311)	31.36	2.526	5.4141	8.3791	1.15	588.29	55.47	45.12	1.23
NCLuF	35.50	0.2625	(311)	33.13	2.526	5.4649	8.3768	1.09	587.81	58.36	39.80	1.46
NCHoF	35.46	0.2858	(311)	30.43	2.528	5.4335	8.3859	1.19	589.74	61.38	45.88	1.33

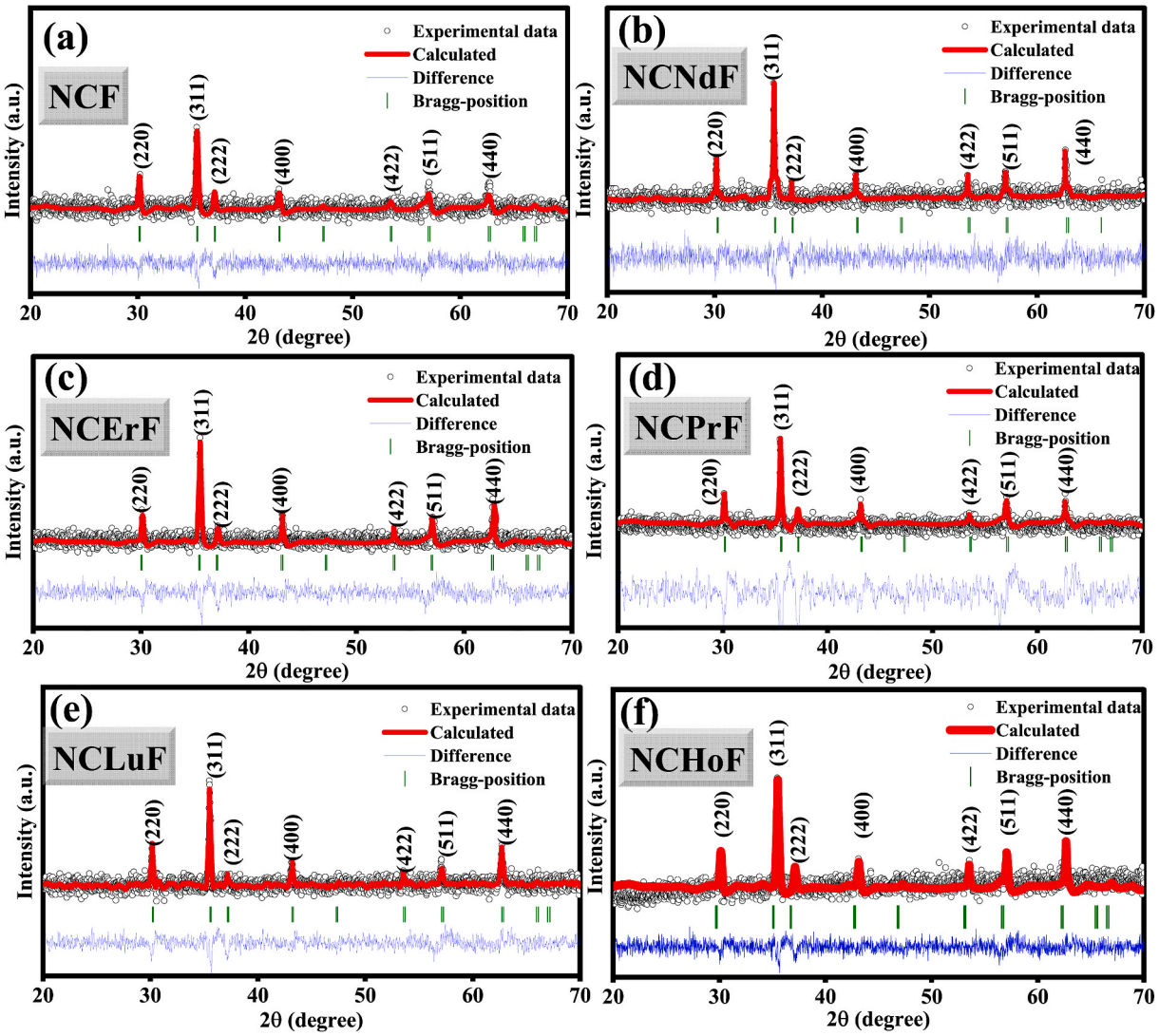


Fig. 3. (a–f) Rietveld refinements XRD patterns for $Ni_{0.2}Co_{0.8}RE_{0.06}Fe_{1.94}O_4$/3 wt% GNP composites.

Table 2
Atomic positions ($x = y = z$), site occupancy (g) and cationic distribution obtained from Rietveld refinement for as-prepared samples.

Ions	NCF		NCNdF		NCErF		NCPrF		NCLuF		NCHoF	
	$x = y = z$	g	$x = y = z$	g	$x = y = z$	g	$x = y = z$	g	$x = y = z$	g	$x = y = z$	g
Ni^{2+}	0.125	0.05	0.125	0.05	0.125	0.05	0.125	0.05	0.125	0.05	0.125	0.05
Ni^{2+}	0.125	0.15	0.125	0.15	0.125	0.15	0.125	0.15	0.125	0.15	0.125	0.15
Co^{2+}	0.125	0.15	0.125	0.15	0.125	0.15	0.125	0.15	0.125	0.15	0.125	0.15
Co^{2+}	0.125	0.65	0.125	0.65	0.125	0.65	0.125	0.65	0.125	0.65	0.125	0.65
Fe^{3+}	0.125	0.80	0.125	0.80	0.125	0.80	0.125	0.80	0.125	0.80	0.125	0.80
Fe^{3+}	0.500	1.14	0.500	1.14	0.500	1.14	0.500	1.14	0.500	1.14	0.500	1.14
Nd^{3+}	----		0.500	0.06	----		----		----		----	
Er^{3+}	----		----		0.500	0.06	----		----		----	
Pr^{3+}	----		----		----		0.500	0.06	----		----	
Lu^{3+}	----		----		----		----		0.500	0.06	----	
Ho^{3+}	----		----		----		----		----		0.500	0.06
O^{2+}	0.255	1.0	0.255	1.0	0.255	1.0	0.255	1.0	0.255	1.0	0.255	1.0
$(Ni^{2+}_{0.05}Co^{2+}_{0.15}Fe^{3+}_{0.8})_A$ $(Ni^{2+}_{0.15}Co^{2+}_{0.65}Fe^{3+}_{1.2})_B O_4$			$(Ni^{2+}_{0.05}Co^{2+}_{0.15}Fe^{3+}_{0.8})_A(Ni^{2+}_{0.15}Co^{2+}_{0.65}Fe^{3+}_{1.14}RE^{3+}_{0.06})_B O_4$ (RE= Nd^{3+}, Er^{3+}, Pr^{3+}, Lu^{3+}, Ho^{3+})									

3.3. TEM micrographs analysis

The TEM micrographs of $Ni_{0.2}Co_{0.8}Fe_2O_4$/3 wt% GNPs and $Ni_{0.2}Co_{0.8}Pr_{0.06}Fe_{1.94}O_4$/3 wt% GNPs are shown in Fig. 6 (a) and (b) respectively. The particle sizes were measured using Image J software, which revealed the spherical-like morphology of particles of synthesized composites. These micrographs also revealed high crystallinity and agglomeration of Ni-Co ferrites and GNPs in synthesized composites. The average particle size observed was 41.39 nm and 39.65 nm of $Ni_{0.2}Co_{0.8}Fe_2O_4$/3 wt% GNPs and $Ni_{0.2}Co_{0.8}Pr_{0.06}Fe_{1.94}O_4$/3 wt% GNPs

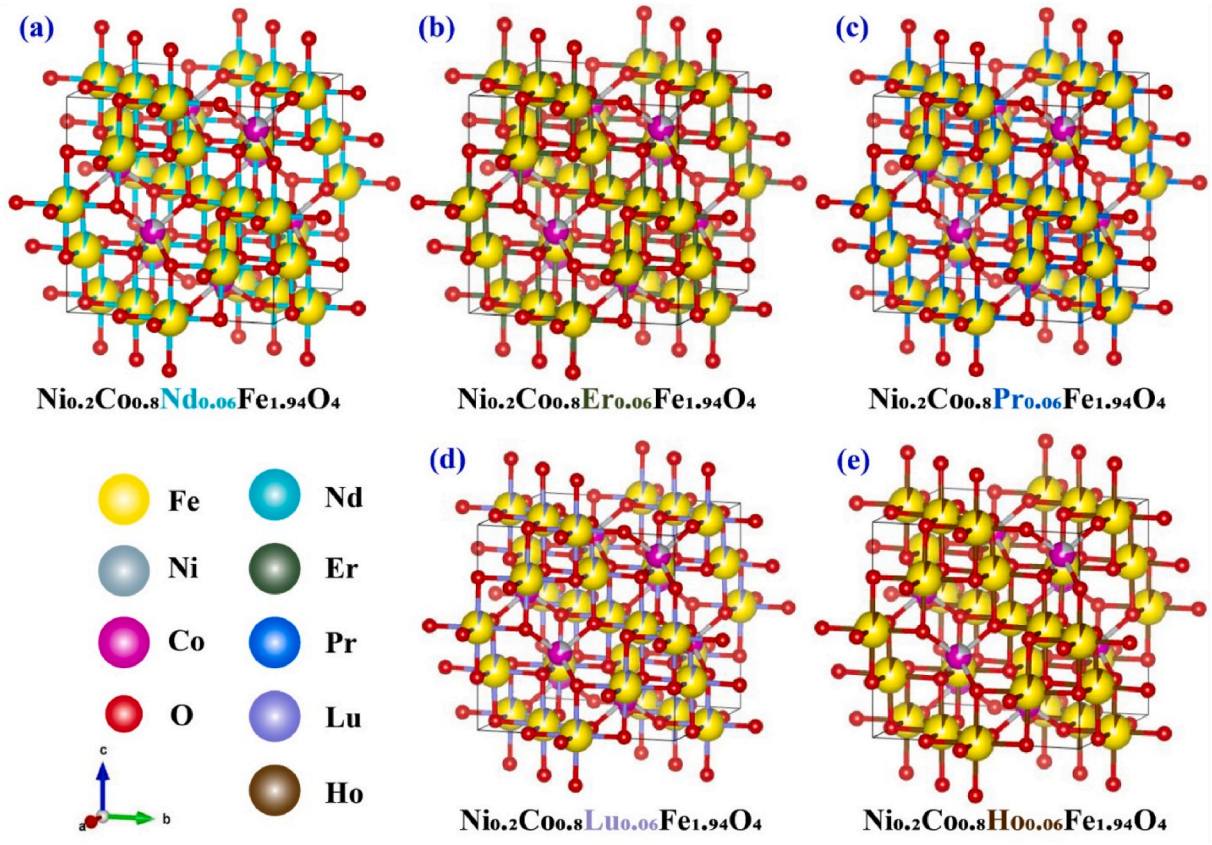


Fig. 4. (a-e) Site occupancy of rare earth elements in unit cell structure of $Ni_{0.2}Co_{0.8}RE_{0.06}Fe_{1.94}O_4$/3 wt% GNP composites.

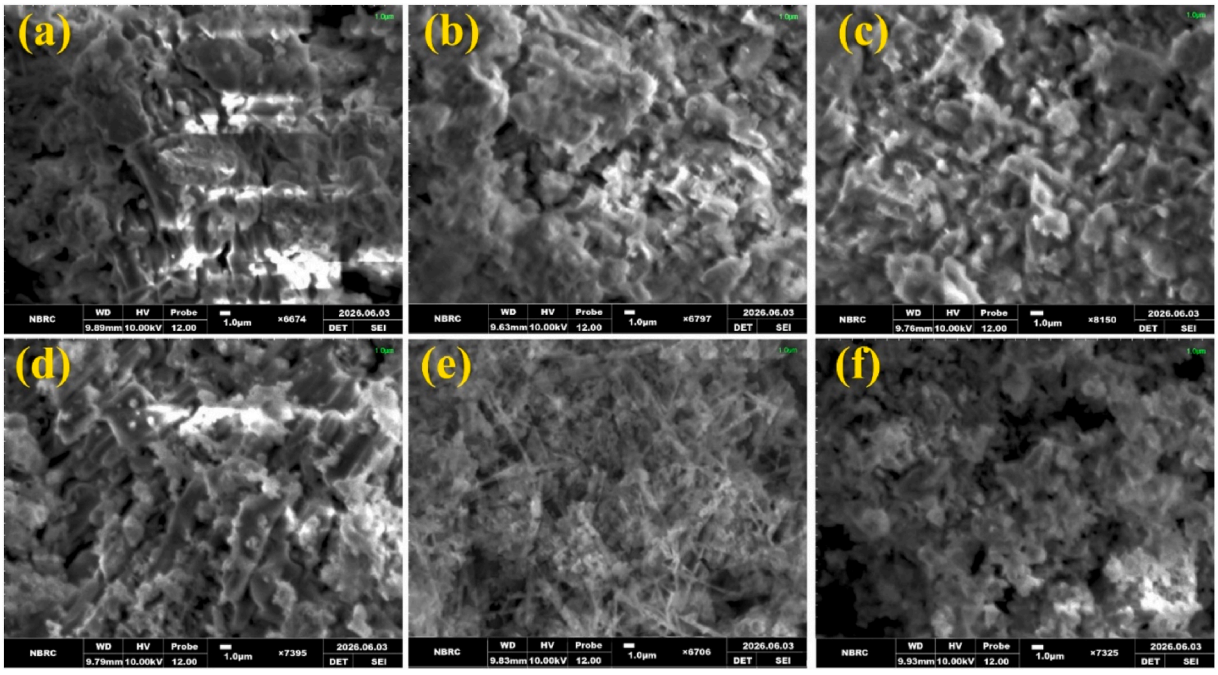


Fig. 5. SEM image of $Ni_{0.2}Co_{0.8}RE_{0.06}Fe_{1.94}O_4$/3 wt% GNP composites.

respectively. The particle size was found higher than crystallite size, because particles consist of crystallites [19].

3.4. Magnetic characteristics

The *M-H* hysteresis loops in Fig. 7(a), show that all rare-earth–doped ($Ni_{0.2}Co_{0.8}RE_{0.06}Fe_{1.94}O_4$/3 wt% GNPs) composites remain soft ferro magnets, but the magnetic properties (saturation magnetization Ms,

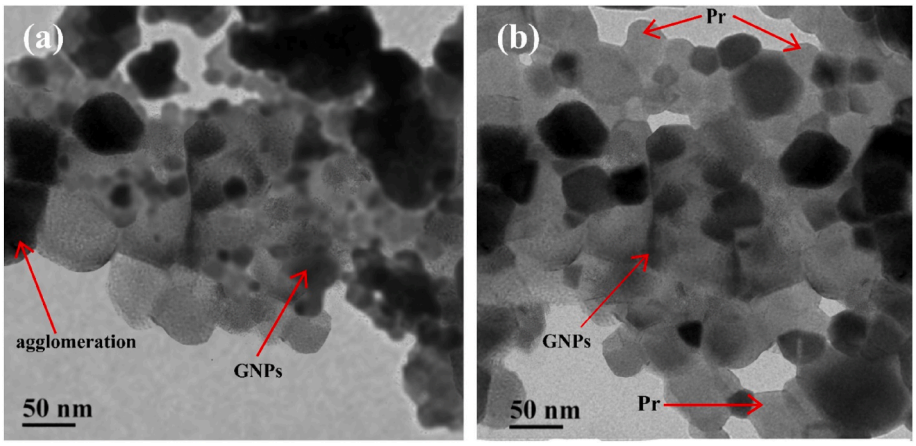


Fig. 6. **(a–b)** TEM micrographs for **(a)** $Ni_{0.2}Co_{0.8}Fe_2O_4$/3 wt% GNPs, **(b)** $Ni_{0.2}Co_{0.8}Pr_{0.06}Fe_{1.94}O_4$/3 wt% GNP nanocomposite.

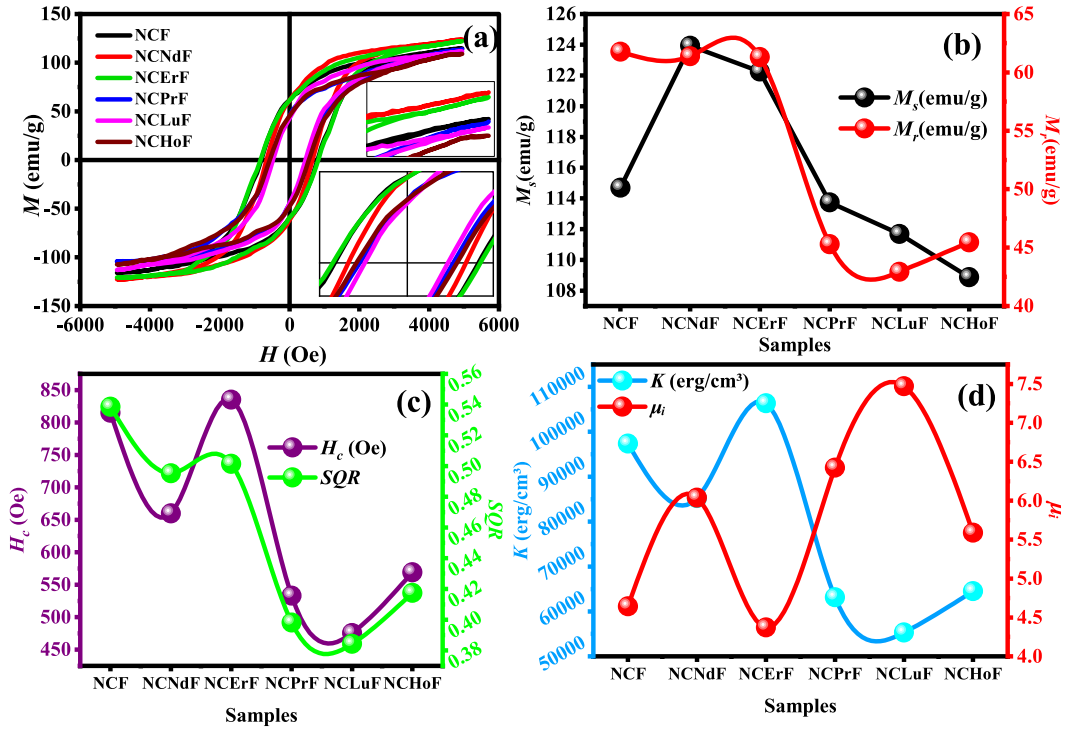


Fig. 7. (a) M − H loop (b) M_s and M_r, (c) H_c and SQR, and (d) K and μ_i vs samples of $Ni_{0.2}Co_{0.8}RE_{0.06}Fe_{1.94}O_4$/3 wt% GNP composites.

remanence Mr, coercivity Hc, squareness ratio Mr/Ms, anisotropy constant K, and initial permeability μi) depend strongly on the dopant as described in Table 3. The magnetic properties are greatly influenced by the doping of rare earth elements due to change in structural parameters and their occupancy at tetra and octahedral sites because the net magnetization is the difference of magnetic moments of B-site and A-site atoms. The super-exchange of cations between these sites also causes the super-exchange interaction in magnetic characteristics [24]. The larger ionic radius results in the expectation that the RE^{3+} ions will occupy B-sites, where they will alter the A–B superexchange interactions which control ferrimagnetism [44]. Besides, the decrease of the crystallite size creates higher surface-to-volume ratio and hence spin canting at the grain boundaries, which may give rise to variations in the saturation magnetization. The role of the ferrite–graphene interfacial structure is also important because it can reduce particle agglomeration as described in SEM images, cause an interfacial strain, and increase the magnetic anisotropy by domain-wall pinning effects. The Nd- and Er-doped composites show higher saturation magnetization than the undoped

Table 3
Magnetic properties of $Ni_{0.2}Co_{0.8}RE_{0.06}Fe_{1.94}O_4$/3 wt% GNP composites.

Sample	M_s (emu/g)	M_r (emu/g)	H_c (Oe)	M_r/M_s	K (10^3 erg/cm^3)	μ_i
NCF	114.7	61.8	815.1	0.54	97.4	4.64
NCNdF	123.9	61.4	660.0	0.49	85.2	6.03
NCErF	122.3	61.7	835.1	0.50	106.4	4.37
NCPrF	113.7	45.3	533.0	0.39	63.1	6.42
NCLuF	111.7	42.9	475.5	0.38	55.3	7.47
NCHoF	108.9	45.5	569.1	0.41	64.5	5.58

composite because of super-exchange interaction, cations distribution among A and B-site, as depicted in Fig. 7(b) [44]. Extracting M_s, M_r and H_c from the M − H curves reveals that the Nd-doped sample has the highest saturation magnetization ($M_s \approx 123.93$ emu/g, $M_r \approx 61.39$ emu/g), exceeding the un-doped (Rare-earth = 0) case ($M_s \approx 114.69$ emu/g, $M_r \approx 61.77$ emu/g). Ho-doping shows the lowest values ($M_s \approx 108.87$ emu/g, $M_r \approx 45.45$ emu/g) [52]. Coercivity ranged from 475.48 Oe to 835.12 Oe in all loops (all samples sharply reversible), with only slight dopant-induced shifts (for example Nd/Er show marginally larger H_c), depicted in Fig. 7(c). In summary, Erbium (and Neodymium) significantly enhances the saturation and remanence magnetization relative to the un-doped composite, whereas Holmium slightly suppresses them; Lu has little effect. These trends reflect how each 4f-ion modifies the ferrite's cation distribution and exchange interactions – Nd^{3+} or Er^{3+} additions can boost net magnetization at low levels, whereas trivalent RE's with closed-shell character (like Lu^{3+}) or strong paramagnetism (Ho^{3+}) tend to dilute the magnetic sublattice [53]. Thus, the data demonstrate that selective RE-doping can be used to engineer the magnetic response of these ferrite/graphene nanocomposites [54]. These differences arise because each RE ion (with its specific magnetic moment and ionic radius) alters the spinel's cation distribution and exchange interactions – for example, Nd^{3+} can increase M_s and H_c at low levels whereas nonmagnetic RE^{3+} often dilute the sublattice. The result is a tunable magnetic profile: by choosing a particular dopant, one can engineer higher saturation (for stronger magnets or memory media) or lower magnetization (for low-loss cores), making these RE–graphene ferrites versatile for targeted applications [55]. The SQR(M_r/M_s) value was found in the range of 0.38 to 0.54, as depicted in Fig. 7(c). The composites doped with rare earth are found to have an M_r/M_s value less than 0.5 which suggest the soft magnetic nature and indicates the presence of single domains while the NCF composite had a value higher than 0.5 which shows the less soft nature and highly anisotropic nature [44]. The anisotropy constant value was found in the range 55.32 erg/cm^3 to 106.35 erg/cm^3 and, the initial permeability was ranged from 4.64 to 7.47 described in Table 3 and Fig. 7(d).

3.5. IV characteristics

The IV characteristics of synthesized samples were measured by Keithley instrument model 2401 at a temperature ranging from 313 K to 773 K as shown in Arrhenius plot in Fig. 8(a). The electrical resistivity of synthesized samples measured by using IV measurements. The DC electrical resistivity influenced by lattice vibrations, drift mobility, and occupancy of ions at lattice sites [56]. The DC resistivity at room temperature was ranged from 3.02×10^7 Ω cm to 3.44×10^9 Ω cm. The DC resistivity decreases with the rise in temperature, at 773 K it ranges from 1.53×10^4 Ω cm to 9.39×10^4 Ω cm as described in Table 4. The

Table 4
Electrical properties of $Ni_{0.2}Co_{0.8}RE_{0.06}Fe_{1.94}O_4$/3 wt% GNPcomposites.

Samples	ρ at room temperature (Ω cm)	ρ at 773 K (Ω cm)	E_a (eV)
$Ni_{0.2}Co_{0.8}Fe_2O_4$/GNPs	5.71×10^8	9.39×10^4	0.711
$Ni_{0.2}Co_{0.8}Nd_{0.06}Fe_{1.94}O_4$/ GNPs	1.10×10^8	4.36×10^4	0.511
$Ni_{0.2}Co_{0.8}Er_{0.06}Fe_{1.94}O_4$/ GNPs	3.44×10^9	4.39×10^4	0.315
$Ni_{0.2}Co_{0.8}Pr_{0.06}Fe_{1.94}O_4$/ GNPs	3.02×10^7	1.53×10^4	0.362
$Ni_{0.2}Co_{0.8}Lu_{0.06}Fe_{1.94}O_4$/ GNPs	3.36×10^8	4.51×10^4	0.341
$Ni_{0.2}Co_{0.8}Ho_{0.06}Fe_{1.94}O_4$/ GNPs	2.07×10^9	4.75×10^4	0.399

decreases in DC resistivity show the semiconducting nature of synthesized composites. The observed variation in the DC resistivity shows that there is no change in oxygen stoichiometry as samples were synthesized in open air and XRD data also confirms it because no secondary phase was observed. The oxygen stoichiometry influence the electronic charge transport properties [57]. The reduction in resistivity was due to rise in drift mobility of charge carriers and lattice vibrations [44,58]. The enhanced lattice vibrations contributed to increase the conductivity of composites [59]. Electrical measurements of ferrites composites depend on the hopping of electrons between ferrous and ferric ions at B-sites. The rise in temperature reduces the resistivity value due to rise in number of hopping pairs of Fe^{2+} and Fe^{3+} which is due to oxygen deficiency at higher temperature [57]. The composites doped with larger ionic radius rare earth elements causes reduction in resistivity. The composites with lower ionic radius dopants having more rare earth element ions replacement at B-site [60]. The smaller the rare earth dopants, the smaller the crystallite size and the greater the number of grain boundaries, causing rise in resistivity [61]. The crystallite size affects the electrical resistivity; they are inversely linked to each other. As the crystallite size decreases, the resistivity rises because of grain boundaries. The smaller the crystallite size, the higher the number of grain boundaries which behave as a barrier to the charge transportation which results in rise of resistivity [62]. The observed trends are consistent with this mechanism as described in Table 1anTable 4. This confirms that the ionic radius of dopants controls the electrical properties of Ni-Co ferrites composites. Furthermore, the crystallite size distribution also influences the mass transport behavior within the synthesized Ni-Co ferrites composites, particularly with respect to oxygen vacancy transport [63]. In nanocrystalline spinel ferrites composites, oxygen vacancies preferentially concentrate at grain boundaries. The transport of oxygen vacancies through grain boundaries may result in local structural disorder and grain boundary degradation, adding to

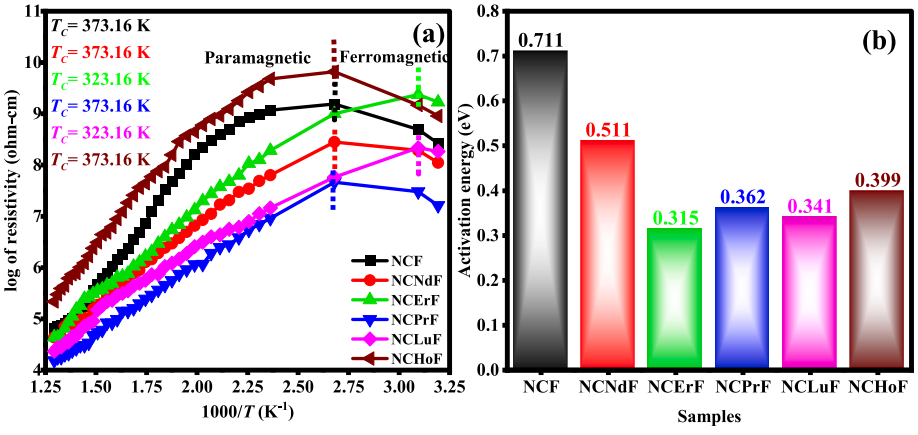


Fig. 8. (a) 1000/T versus log of resistivity and (b) activation energy of $Ni_{0.2}Co_{0.8}RE_{0.06}Fe_{1.94}O_4$/3 wt% GNP composites.

the modification of electronic properties of the composites. From all the synthesized composites, $Ni_{0.2}Co_{0.8}Pr_{0.06}Fe_{1.94}O_4$/GNPs shows the least resistivity and minimal lattice distortion, which make it promising candidate as electrode material due to charge transport [46]. The Curie temperature also observed in the Arrhenius plot, which is marked by dotted line in Fig. 8(a). The Curie point shows the conversion of synthesized composites from ferromagnetic nature to paramagnetic nature. Activation energy was ranged from 0.341 eV to 0.711 eV as described in Fig. 8(b). The activation energy of synthesized composites varies with the lattice distortions. It had least value for the composites having least lattice distortions and dopants with large ionic radius [64]. As the crystallite size decreases, the surface atoms experience compressive stress inward, which leads to contraction of crystal lattice, evident by lattice parameter presented in Table 1. Such compression widens the band gap of synthesized material and consistent with their higher activation energy[63]. The variation in the resistivity of the composites is, therefore, explained not only by the electron hopping mechanism between Fe^{2+} and Fe^{3+} ions at B-sites, but also by the multiplicity of the grain boundary scattering of electrons in the smaller crystallites, surface lattice compression (as a result of the high crystallite size), and the transport of oxygen vacancies along the grain boundaries, intrinsic parameters of which depend on the crystallite size and its distribution in the synthesized nanocomposites. The composites $Ni_{0.2}Co_{0.8}Pr_{0.06}Fe_{1.94}O_4$/GNPs shows the most effective and suitable value among the all composites for electrode material applications. The $Ni_{0.2}Co_{0.8}Pr_{0.06}Fe_{1.94}O_4$/GNPs composite shows the most suitable IV characteristics due to its low resistivity and activation energy, which support the charge transfer phenomena in electrodes.

3.6. Dielectric characteristics

Fig. 9(a) shows that the dielectric constant (real permittivity ε') of all $Ni_{0.2}Co_{0.8}RE_{0.06}Fe_{1.94}O_4$/GNPs composites decreases monotonically with increasing frequency – a behavior characteristic of spinel ferrites subject to Maxwell–Wagner interfacial polarization. At low frequencies, space-charge accumulation at grain boundaries yields the highest ε', whereas at higher frequencies the dipolar and interfacial polarizations cannot follow the field and ε' levels off [12]. Among the rare-earth substitutions, the Lu^{3+}-doped sample consistently exhibits the largest ε' across the measured range, while the pure sample has the smallest ε'. This ordering suggests that the specific RE–ion strongly influences polarization: Ho^{3+} (with relatively smaller ionic radius and a high 4f magnetic moment) appears to enhance the lattice polarizability more than Pr^{3+} (larger radius, weaker moment). In fact, rare-earth doping is known to increase the dielectric constant of ferrites, and here the magnitude of ε' enhancement depends on the electronic configuration of rare earth elements and ionic size [10,65]. The presence of graphene nanoplatelets further boosts ε' at low frequency by creating additional interfacial polarization [1,66].

The dielectric tangent loss (*tan δ*) also decreases with frequency for all samples, as plotted in Fig. 9(b). Each sample shows maximal *tan δ* at the lowest frequencies, which falls off sharply and becomes very small above ~10^5 Hz [8]. This behavior mirrors the ε' dispersion: at low frequency, space-charge polarization and charge hopping produce large energy dissipation, while at high frequency dipolar relaxation and hopping cannot keep up so losses drop to a baseline [8,12]. The Lu-doped ferrite exhibits the highest *tan δ* at low frequency (consistent with its larger ε'), whereas the pure sample had the lowest losses. Nd- and Ho-doped samples show moderate *tan δ* values, commensurate with their intermediate ε'. In spinel ferrites, dielectric loss is largely due to hopping of charge between transition-metal ions (e.g. $Fe^{2+}\leftrightarrow Fe^{3+}$, $Co^{2+}\leftrightarrow Co^{3+}$, $Ni^{2+}\leftrightarrow Ni^{3+}$) on the octahedral sites [8,60]. Thus, substitution with different R^{3+} cations (which alter the carrier mobility, defect structure, and hopping barriers) modulates tan δ in tandem with ε'. At high frequencies all samples converge to very low *tan δ* values, in agreement with Koop's phenomenological model and the Maxwell–Wagner relaxation picture [8,67]. Overall, the rare-earth trend (higher ε' and lower *tan δ* for Ho vs. lower ε' and higher *tan δ* for Pr) implies that Ho^{3+} substitution favors stronger interfacial polarization and/or higher resistivity than Pr^{3+}. These trends are qualitatively consistent with other reports on RE-doped ferrites [8,66,68], where larger magnetic moment or smaller ionic radius ions tend to enhance

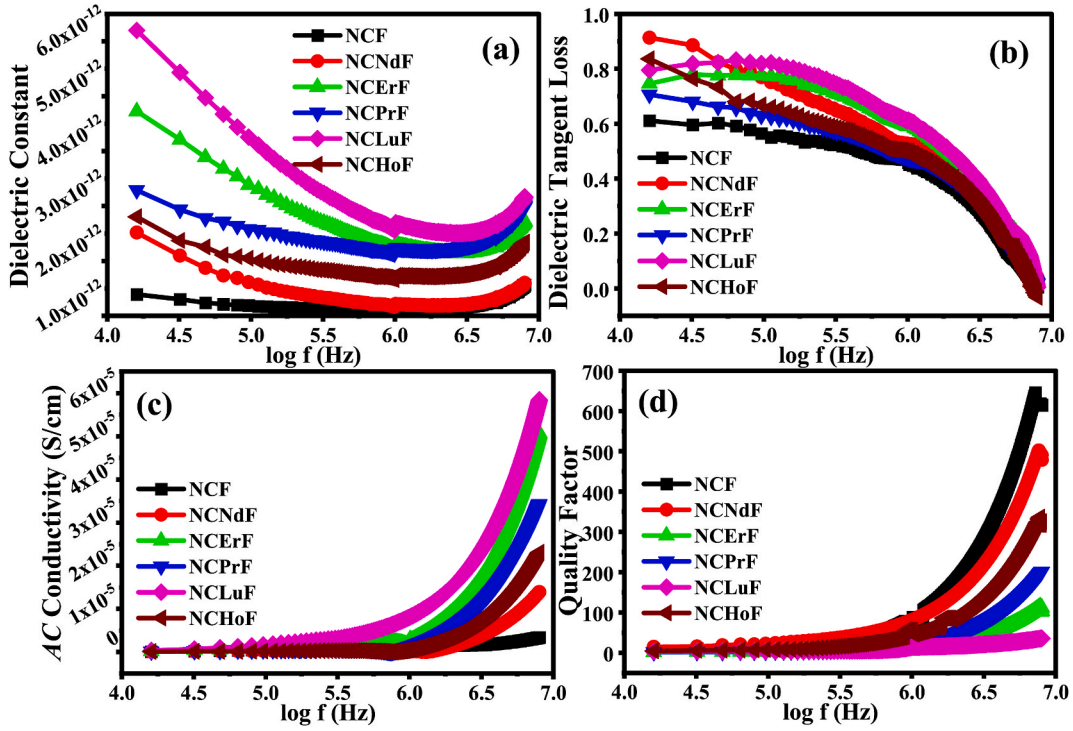


Fig. 9. Log of frequency versus (a) dielectric constant, (b) Dielectric tangent loss, (c) *AC* conductivity and (d) Quality factor of $Ni_{0.2}Co_{0.8}RE_{0.06}Fe_{1.94}O_4$/3 wt% GNP composites.

dielectric response and introduce distinct dispersion in ε' and *tan* δ. The observed dispersion of ε' and *tan* δ with frequency is well documented in ferrites, and the effects of RE–ion size/moment on permittivity have been discussed in the literature [68,69]. Our data demonstrate that Lu^{3+} substitution yields the strongest dielectric polarization in this Ni–Co spinel system, while pure composite gives the weakest, illustrating the interplay of ionic radius and 4f electronic structure on dielectric behavior.

AC conductivity in Fig. 9(c) showed a clear and significant increase with frequency, consistent with the well-established behavior observed in many dielectric and conductive materials. The Maxwell-Wagner model explains this behavior, frequency dependent conductivity. According to this model, grain boundaries play vital role at low frequencies, due to this electron hopping is low at low frequencies. At higher frequencies, the hoping of electrons between ferric and ferrous ions occur which give rise to the conductivity [60,67]. The $Ni_{0.2}Co_{0.8}Lu_{0.06}Fe_{1.94}O_4$/3 wt% GNPs composite exhibits the highest value of AC conductivity among the synthesized composites.

In Fig. 9(d), Quality factor is depicted versus log of frequency. At low frequency range quality factor value is low and it increases with the rise in frequency. The higher value of quality factor indicates the minimal energy losses at higher frequencies. This behavior aligns with the dielectric tangent loss, its value is high at low frequency and decreases with the rise in frequency, both are inversely linked with each other, as reported in literature [44,70]. Due to this behavior, high Quality factor value at high frequency, these synthesized composites are suitable for high-frequency applications, because less energy dissipation into heat is required in them, like resonators. Due to low energy losses at higher frequencies, these composites also favorable as a dielectric medium in capacitive devices, as a lower dielectric constant implies less ability to store electrical energy at higher frequencies. Energy losses were found higher in low frequency range because of interfacial polarization [44]. At higher frequencies, grain boundaries becomes active and contribute in charge transportation and energy dissipations decreases, leading to a lower tan δ value. This behavior is consistent with similar findings in materials exhibiting complex polarization mechanisms [71,72]. The frequency-dependent dielectric loss is particularly important for applications such as microwave absorbers and high-frequency capacitors, where low energy dissipation is desirable [73].

4. Conclusions

The present study demonstrates the successful synthesis and characteristics analysis of rare-earth-modified nickel–cobalt ferrite nanocomposites integrated with GNPs, offering a unique combination of structural integrity, dielectric responsiveness, and improved electrical performance. The materials were synthesized through a sol-gel autocombustion approach, which ensured uniform incorporation of graphene nanoplatelets into the ferrite matrix. The XRD analysis confirms that the $Ni_{0.2}Co_{0.8}Pr_{0.06}Fe_{1.94}O_4$/3 wt% GNPs composite was found to be the most promising candidate as electrode material because of its optimized crystallite size value of 31.4 nm. SEM analysis confirms the successful synthesis of a nanostructured and porous ferrite-graphene composite. The composites doped with rare earth are found to have M_r/M_s value less than 0.5 which suggest the soft magnetic nature. The $Ni_{0.2}Co_{0.8}Pr_{0.06}Fe_{1.94}O_4$/3 wt% GNP composite shows the most suitable IV characteristics due to its low resistivity (3.02×10^7 Ω cm) and activation energy (0.362 eV), which support the charge transfer phenomena in electrodes. The dielectric constant and dielectric tangent loss decreases with the increases in frequency while AC conductivity and Quality factor increases. The composites $Ni_{0.2}Co_{0.8}Pr_{0.06}Fe_{1.94}O_4$/GNPs show the most promising characteristics among all doped Ni-Co ferrite/GNP composites for electrode material applications.

CRediT authorship contribution statement

Sana Riasat: Writing – original draft. **Zeshan Munir:** Writing – review & editing. **Maria Akhtar:** Formal analysis. **Le Duc Tung:** Writing – review & editing. **Rawiyah Alkahtani:** Investigation. **Ohud Alzaidi:** Validation, Visualization. **M.S. Al-Buriahi:** Validation. **Salah Knani:** Visualization. **Shahir Hussain:** Validation. **Nguyen Thi Kim Thanh:** Writing – review & editing. **Muhammad Imran Arshad:** Supervision, Writing – review & editing.

Declaration of competing interest

The authors declare that they have no known competing financial interests or personal relationships that could have appeared to influence the work reported in this paper.

Acknowledgement

The authors express their gratitude to Princess Nourah bint Abdulrahman University Researchers Supporting Project number (PNURSP2026R943), Princess Nourah bint Abdulrahman University, Riyadh, Saudi Arabia. The authors extend their appreciation to the Deanship of Scientific Research at Northern Border University, Arar, KSA for funding this research work through the project number (NBU-CRP-2026-2483).

References

[1] A. Ur Rehman, M.I. Arshad, N. Amin, Transport and magnetic properties of Zn0.5Co0.25Cu0.25Ho0.037Fe1.963O4/Graphene nanoplatelets nanocomposites, Ceram. Int. 50 (2024) 55940–55952, https://doi.org/10.1016/J.CERAMINT.2024.11.004.

[2] J. Liang, Z. Li, F. Ye, Y. Cao, Y. An, X. Fan, Q. Song, Graphene-skinned fiber with fine-tunable electrical resistance via radical and substrate engineering for electromagnetic-thermal fabric, Nano-Micro Lett. 18 (2026) 263, https://doi.org/10.1007/s40820-026-02117-8.

[3] S.S. Wanjari, D.V. Nandanwar, K.G. Rewatkar, A.V. Gongal, Investigating impact of Ni-Cd substitution on structural magnetic and optical properties of nanosize Al ferrites, Heliyon 10 (2024) e39734, https://doi.org/10.1016/j.heliyon.2024.e39734.

[4] M.A. Warsi, M. Hashim, I. Nadeem, M.A. Yameen, M.N. Akram, M. ul Mannan Shah, M.I. Arshad, Enhanced microwave absorption in La^3+Doped Mn-Co-Cd spinel ferrites via magneto-dielectric coupling, Surf. Interfaces 80 (2026) 108248, https://doi.org/10.1016/j.surfin.2025.108248.

[5] M.A. Almessiere, N.A. Algarou, Y. Slimani, D.S. Klygach, A. Baykal, A.D. Korkmaz, T.I. Zubar, M.V. Silibin, M.G. Vakhitov, A. Ui-Hamid, S.V. Trukhanov, A. V. Trukhanov, Structure, magnetic, and electrodynamic properties of SrInxFe12-xO4/Ni0.5Zn0.5Fe2O4 composites at low temperature, J. Am. Ceram. Soc. 107 (2024) 4936–4948, https://doi.org/10.1111/jace.19798.

[6] T. Hong, J. Guan, W. Zhou, S. Tan, Z. Cai, Sustainable methods for the synthesis of chiral nanomaterials, Cell Rep. Phys. Sci. 6 (2025) 102785, https://doi.org/10.1016/j.xcrp.2025.102785.

[7] L.Y. Matzui, A.V. Trukhanov, O.S. Yakovenko, L.L. Vovchenko, V.V. Zagorodnii, V. V. Oliynyk, M.O. Borovoy, E.L. Trukhanova, K.A. Astapovich, D.V. Karpinsky, S. V. Trukhanov, Functional magnetic composites based on hexaferrites: correlation of the composition, magnetic and high-frequency properties, Nanomaterials 9 (2019) 1720, https://doi.org/10.3390/nano9121720.

[8] Z. Latif, A.U. Rehman, N. Amin, M.I. Arshad, R. Marzouki, Graphene nanoplatelets (GNPs): a source to bring change in the properties of Co-Ni-Gd-ferrite/GNP nanocomposites, RSC Adv. 13 (2023) 34308–34321, https://doi.org/10.1039/d3ra02080k.

[9] W. Ci, H. Yang, W. Xue, R. Yang, B. Lv, P. Wang, R.-W. Li, X.-H. Xu, Thickness-dependent and strain-tunable magnetism in two-dimensional van der Waals VSe2, Nano Res. 15 (2022) 7597–7603, https://doi.org/10.1007/s12274-022-4400-9.

[10] A. Hameed, A. Asghar, S. Shabbir, I. Ahmed, A.K. Tareen, K. Khan, G. Hussain, M. Y. Awaji, H. Anwar, A detailed investigation of rare earth lanthanum substitution effects on the structural, morphological, vibrational, optical, dielectric and magnetic properties of Co-Zn spinel ferrites, Front. Chem. 12 (2024) 1–20, https://doi.org/10.3389/fchem.2024.1433004.

[11] W. Yu, C. Ma, Y. Ma, G. Ma, H. Wang, Y. Zhou, H. Guo, Boosting electromagnetic wave absorbing capacity of Al2O3 coating through in situ generating nano TiO1.81 from Ti2AlC MAX phases, Adv. Funct. Mater. 35 (2025) 2504393, https://doi.org/10.1002/adfm.202504393.

[12] X. Zhou, X. Wen, Y. Liu, P. Li, H. Fan, Q. Wang, Dislocation-induced space charge effects in electrode materials of lithium-ion batteries, Acta Mater. 303 (2026) 121746, https://doi.org/10.1016/j.actamat.2025.121746.

[13] N. Yang, H. Gao, S. Ju, Z. Zhang, Y. Zhao, X.-W. Guo, S. Xing, J. Liu, J. Zhang, K. Duan, Y. He, Achieving broadband electromagnetic absorption in laminated composites through progressive Bayesian optimization, Composites, Part B Eng. 307 (2025) 112882, https://doi.org/10.1016/j.compositesb.2025.112882.
[14] Z. Yang, J. Yi, F. Li, Z. Li, L. Ye, B. Li, J. Christensen, Static mechanical cloaking and camouflage from disorder, Nat. Commun. 16 (2025) 8858, https://doi.org/10.1038/s41467-025-63939-5.
[15] R. Siddiqui, M. Rani, A. Ibrahim, A.A. Shah, A. Razaq, S. Bano, M. Ajmal Khan, Enhanced specific capacitance of supercapacitors using wide band gap NdCrO3 and NdCrO3/graphene oxide nanocomposites, J. Rare Earths 43 (2025) 2231–2237, https://doi.org/10.1016/j.jre.2024.08.023.
[16] P. Zhang, X. Yue, X. Jiang, Y. Sun, Y. Wang, Study on the influence of multi-energy field combined surface modification on the subsurface microstructure evolution of AA7075 aluminum alloy, Mater. Charact. 219 (2025) 114644, https://doi.org/10.1016/j.matchar.2024.114644.
[17] Y. Slimani, M.A. Almessiere, A. Baykal, D.S. Klygach, S.V. Trukhanov, A. V. Trukhanov, A. Ul-Hamid, Structural, magnetic, electromagnetic, and hyperfine interactions of rare earth Ho3+ doped in mixed Co–Ni spinel ferrites, Appl. Phys. A 131 (2025) 455, https://doi.org/10.1007/s00339-025-08576-x.
[18] A. Aslam, A. Razzaq, S. Naz, N. Amin, M.I. Arshad, M.A.U. Nabi, A. Nawaz, K. Mahmood, A. Bibi, F. Iqbal, M. Shakil, Z. Farooq, M.Z. Iqbal, S.S. Haider, A. ur Rehman, Impact of lanthanum-doping on the physical and electrical properties of cobalt ferrites, J. Supercond. Nov. Magn. 34 (2021) 1855–1864, https://doi.org/10.1007/s10948-021-05802-4.
[19] M. Imran Iqra, Z. Munir, N. Amin, M. Akhtar, M.S. Al-buriahi, A.M. Binzowaimil, M. Al-hmoud, Enhanced absorption-dominant EMI shielding effectiveness by applied magnetic fields, Ceram. Int. 52 (2026) 23433–23446, https://doi.org/10.1016/j.ceramint.2026.03.395.
[20] P. Sowjanya, N. Pavan Kumar, A. Chelvane, M.V. Ramana Reddy, Comparative study between Ni–Co ferrite and multi rare earth element doped Ni–Co ferrite, Mater. Sci. Eng. B 297 (2023) 116753, https://doi.org/10.1016/j.mseb.2023.116753.
[21] A. Lassoued, J.F. Li, Magnetic and photocatalytic properties of Ni–Co ferrites, Solid State Sci. 104 (2020) 106199, https://doi.org/10.1016/j.solidstatesciences.2020.106199.
[22] Y. Zhang, Y. Wang, H. Yu, J. Sun, Z. Shi, X. Zhang, Electroplated Ni/Cu/Ni coatings on sintered Nd-Fe-B magnets: influence of layer structure on the anti-corrosion, magnetic and mechanical properties, Appl. Surf. Sci. 737 (2026) 166871, https://doi.org/10.1016/j.apsusc.2026.166871.
[23] S.V. Trukhanov, A.V. Trukhanov, V.G. Kostishyn, L. V Panina, A.V. Trukhanov, V. A. Turchenko, D.I. Tishkevich, E.L. Trukhanova, O.S. Yakovenko, L.Y. Matzui, D. A. Vinnik, D. V Karpinsky, Effect of gallium doping on electromagnetic properties of barium hexaferrite, J. Phys. Chem. Solids 111 (2017) 142–152, https://doi.org/10.1016/j.jpcs.2017.07.014.
[24] Z. Munir, M.I. Arshad, N. Amin, Iqra, M. Akhtar, M.S. Al-Buriahi, A. M. Binzowaimil, M. Al-Hmoud, Optimized EMI shielding effectiveness of co-cu-gd spinel ferrites reinforced with graphene nanoplatelets, Ceram. Int. 52 (2026) 29338–29348, https://doi.org/10.1016/j.ceramint.2026.05.013.
[25] M.A. Almessiere, A.V. Trukhanov, F.A. Khan, Y. Slimani, N. Tashkandi, V. A. Turchenko, T.I. Zubar, D.I. Tishkevich, S.V. Trukhanov, L.V. Panina, A. Baykal, Correlation between microstructure parameters and anti-cancer activity of the [Mn0.5Zn0.5](EuxNdxFe2-2x)O4 nanoferrites produced by modified sol-gel and ultrasonic methods, Ceram. Int. 46 (2020) 7346–7354, https://doi.org/10.1016/j.ceramint.2019.11.230.
[26] M.A. Almessiere, Y. Slimani, H. Güngüneş, A. Baykal, S.V. Trukhanov, A. V. Trukhanov, Manganese/Yttrium codoped strontium nanohexaferrites: evaluation of magnetic susceptibility and Mossbauer spectra, Nanomaterials 9 (2019), https://doi.org/10.3390/nano9010024.
[27] B. Zheng, J. Fan, B. Chen, X. Qin, J. Wang, F. Wang, R. Deng, X. Liu, Rare-earth doping in nanostructured inorganic materials, Chem. Rev. 122 (2022) 5519–5603, https://doi.org/10.1021/acs.chemrev.1c00644.
[28] S. Sharma, M.K. Verma, N.D. Sharma, N. Choudhary, S. Singh, D. Singh, Rare-earth doped Ni–Co ferrites synthesized by Pechini method: cation distribution and high temperature magnetic studies, Ceram. Int. 47 (2021) 17510–17519, https://doi.org/10.1016/j.ceramint.2021.03.069.
[29] M. Mansour, M. Bechelany, R. Habchi, C. Eid, Influence of graphene oxide doping on the morphology and the magnetic properties of Ni0.8Gd0.2Fe2O4 nanofibers prepared by electrospinning, Phys. Lett. 381 (2017) 658–662, https://doi.org/10.1016/j.physleta.2016.12.014.
[30] M.N. Akhtar, M. Yousaf, Y. Lu, M.Z. Mahmoud, J. Iqbal, M.A. Khan, M. U. Khallidoon, S. Ullah, M. Hussien, Magnetic, structural, optical band alignment and conductive analysis of graphene-based REs (Yb, Gd, and Sm) doped NiFe2O4 nanocomposites for emerging technological applications, Synth. Met. 284 (2022) 1–9, https://doi.org/10.1016/j.synthmet.2021.116994.
[31] V. Bhuvaneshwari, N. Lenin, C. Shiva, M. Kathirvel, V. Ragavendran, A. Rajeshwari, B. Guruprakash, G.G.V. Kumar, Influence of gadolinium doped in nickel nanoferrites on structural, optical, electrical, and magnetic properties, Mater. Sci. Eng. B 288 (2023) 116184, https://doi.org/10.1016/j.mseb.2022.116184.
[32] D.A. Vinnik, V.E. Zhivulin, D.P. Sherstyuk, A.Y. Starikov, P.A. Zezyulina, S. A. Gudkova, D.A. Zherebtsov, K.N. Rozanov, S.V. Trukhanov, K.A. Astapovich, A.S. B. Sombra, D. Zhou, R.B. Jotania, C. Singh, A.V. Trukhanov, Ni substitution effect on the structure{,} magnetization{,} resistivity and permeability of zinc ferrites, J. Mater. Chem. C 9 (2021) 5425–5436, https://doi.org/10.1039/D0TC05692H.
[33] J. Li, M. Yousaf, Q. Hayat, M. Akbar, A. Noor, M.A.K.Y. Shah, F. Qi, Y. Lu, Effect of rare earth Nd3+ doping contents on physical, structural, and magnetic properties of Co–Ni spinel ferrite nanoparticles, J. Rare Earths 41 (2023) 1746–1753, https://doi.org/10.1016/j.jre.2022.12.007.
[34] Shubhra, R.K. Singh, N. Kumar, V. Kumar, S.B. Das, M.M.H. Siddiqui, Impact of doping Gd3+rare earth ion on structural, magnetic, and optical properties of cobalt and nickel ferrite nanomaterials, Appl. Phys. A 127 (2021) 861, https://doi.org/10.1007/s00339-021-05011-9.
[35] W. Xue, P. Wang, W. Ci, Y. Guo, J. Qu, Z. Zeng, T. Liu, R. He, S. Cheng, X. Xu, Emergence of sliding ferroelectricity in naturally parallel-stacked multilayer ReSe (2) semiconductor, Nat. Commun. 16 (2025) 6313, https://doi.org/10.1038/s41467-025-61756-4.
[36] S.M. Abdulkareem, R.M. Alsaffar, G.H.A. Razzaq, J.H. Mohammed, T.M. Awad, M. A. Alheety, L.A. Mohammed, A.H. Mageed, E.M. Ali, A.H. Dalaf, S. Rustagi, S. Ghotekar, Effect of direct and indirect in-situ sonochemical synthesis methods of MWCNTs–CoNiFerrite on the hydrogen storage, J. Sol. Gel Sci. Technol. 111 (2024) 979–988, https://doi.org/10.1007/s10971-024-06502-w.
[37] A. Monshi, M.R. Foroughi, M.R. Monshi, Modified scherrer equation to estimate more accurately nano-crystallite size using XRD, World J. Nano Sci. Eng. 2 (2012) 154–160, https://doi.org/10.4236/wjnse.2012.23020.
[38] A.U. Rehman, N. Amin, M.B. Tahir, M. Ajaz un Nabi, N.A. Morley, M. Alzaid, M. Amami, M. Akhtar, M.I. Arshad, Evaluation of spectral, optoelectrical, dielectric, magnetic, and morphological properties of RE3+ (La3+, and Ce3+) and Co2+ co-doped Zn0.75Cu0.25Fe2O4 ferrites, Mater. Chem. Phys. 275 (2022) 125301, https://doi.org/10.1016/j.matchemphys.2021.125301.
[39] A.V. Trukhanov, V.A. Turchenko, V.G. Kostishin, F. Damay, F. Porcher, N. Lupu, B. Bozzo, I. Fina, S. Polosan, M.V. Silibin, M.M. Salem, D.I. Tishkevich, S. V. Trukhanov, The origin of the dual ferroic properties in quasi-centrosymmetrical SrFe12−xInxO19 hexaferrites, J. Alloys Compd. 886 (2021) 161249, https://doi.org/10.1016/j.jallcom.2021.161249.
[40] A. Murugan, A. Fatehmulla, S. Priya, S.S. Han, S. Babu, C. Rohit, S. Bharathkumar, Optimizing the photocatalytic properties Er-doped bismuth ferrite for the degradation of mixed dyes under sunlight irradiation, Surf. Interfaces 54 (2024) 105239, https://doi.org/10.1016/j.surfin.2024.105239.
[41] M.M. Ilyas, A. Manzoor, A. Shahzad, M.A. Khan, M.N. Rasul, Cd-Zn-Ni ferrites/GNP nanocomposite electrode for high-performance supercapacitors, Ceram. Int. (2025) 4–7, https://doi.org/10.1016/j.ceramint.2025.01.589.
[42] S. Yuan, F. Ren, G. Zhu, C. Li, W. Tian, Y. Jin, Z. Guo, Z. Chen, P. Ren, Puffed millet activated carbon supported CoNi layered double hydroxides for high-performance supercapacitor electrode material, J. Energy Storage 146 (2026) 120151, https://doi.org/10.1016/j.est.2025.120151.
[43] Q. Ke, J. Wang, Graphene-based materials for supercapacitor electrodes – a review, J. Mater. 2 (2016) 37–54, https://doi.org/10.1016/j.jmat.2016.01.001.
[44] Z. Munir, N. Amin, M.I. Arshad, Magneto-dielectric properties of GNPs modified Co0.7Cu0.3Ho0.1Fe1.9O4 nanocomposites with the balanced dielectric-magnetic loss for high frequency applications, Ceram. Int. 51 (2025) 34440–34454, https://doi.org/10.1016/J.CERAMINT.2025.05.169.
[45] U. Saha, R. Jaiswal, T.H. Goswami, P.K. Maji, Cobalt ferrite (CoFe2O4)–activated carbon fabric (ACF) based composite electrode material for supercapacitor application, J. Energy Storage 99 (2024) 113218, https://doi.org/10.1016/j.est.2024.113218.
[46] R. Lakra, R. Kumar, P.K. Sahoo, D. Thatoi, A. Soam, A mini-review: Graphene based composites for supercapacitor application, Inorg. Chem. Commun. 133 (2021) 108929, https://doi.org/10.1016/j.inoche.2021.108929.
[47] T. Kousar, M. Aadil, S. Zulfiqar, S.M. Ibrahim, S. Mubeen, W. Hassan, K. Shafiq, F. Mahmood, Facile synthesis of graphene anchored rare earth doped mixed metal ferrite nanorods: a potential candidate for azo dye mineralization, J. Rare Earths 42 (2024) 907–916, https://doi.org/10.1016/j.jre.2023.07.002.
[48] S. Nayak, S.S. Nayak, A.A. Kittur, S. Nayak, D.R. Joshi, Synthesis, fabrication, and performance evaluation of lanthanum doped nickel cobalt ferrite electrode for supercapacitors in energy storage applications, J. Energy Storage 101 (2024) 113918, https://doi.org/10.1016/j.est.2024.113918.
[49] M.I. Arshad, K. Mehmood, N. Amin, N.A. Morley, N.T.K. Thanh, Superior magnetodielectric properties of CoZnNd ferrites/GNPs composite materials for potential applications, Compos. Commun. 39 (2023) 101571, https://doi.org/10.1016/j.coco.2023.101571.
[50] C. Yang, X. Xin, W. Zhao, C. Lin, L. Liu, Y. Liu, J. Leng, Highly programmable 4D printed multi-shape gradient metamaterials and multifunctional devices, Int. J. Extrem. Manuf. 7 (2025) 55504, https://doi.org/10.1088/2631-7990/add8ca.
[51] P. Akhtar, M.N. Akhtar, M.A. Baqir, A. Ahmad, M.U. Khallidoon, M. Farhan, M. A. Khan, Structural and magnetic evaluations of rare-earths (Tb, Pr, Ce, Gd, Y)-doped spinel ferrites for high frequency and switching applications, J. Mater. Sci. Mater. Electron. 32 (2021) 7692–7703, https://doi.org/10.1007/s10854-021-05487-4.
[52] T. Rajender, K.C.B. Naidu, D.B. Basha, S. Samanta, L.S.S. Reddy, Magnetic, dielectric and thermal study of CoNiFe2O4 nanoparticles, Nano-Struct. Nano-Objects 38 (2024) 101167, https://doi.org/10.1016/j.nanoso.2024.101167.
[53] M.A. Almessiere, A. Baykal, Y. Slimani, H. Güngüneş, A.D. Korkmaz, D.S. Klygach, S.V. Trukhanov, T.I. Zubar, A.V. Trukhanov, Impact of palladium ions doping on structural, magnetic, and electromagnetic properties and hyperfine interactions of Co-Ni nanospinel ferrites, Appl. Phys. A 130 (2024) 932, https://doi.org/10.1007/s00339-024-08092-4.
[54] J.C. Góes, S.D. Figueiró, K.D.A. Sabóia, Y.L. Nunes, A.C.H. Barreto, P.B. Fechine, S. Devesa, A.S. Sombra, M.A. Valente, S.R. Gavinho, M.P. Graça, Exploring dielectric and magnetic properties of Ni and Co ferrites through biopolymer composite films, Magnetochemistry 10 (2024) 20, https://doi.org/10.3390/magnetochemistry10040020.

[55] L. Shao, A. Sun, Y. Zhang, L. Yu, N. Suo, Z. Zuo, Comparative study on the structure and magnetic properties of Ni-Mg-Co ferrite doped with Al and rare earth elements, J. Mater. Sci. Mater. Electron. 32 (2021) 5339–5352, https://doi.org/10.1007/s10854-020-05161-1.

[56] M.R. Saleem, M.I. Arshad, N. Amin, Microstructural and magneto-dielectric properties of Cd-Zn-La iron oxide/graphene Nanoplatelets(GNPs) composites, Mater. Sci. Eng. B 320 (2025) 118440, https://doi.org/10.1016/j.mseb.2025.118440.

[57] I.O. Troyanchuk, S.V. Trukhanov, H. Szymczak, K. Baerner, Effect of oxygen content on the magnetic and transport properties of Pr0.5Ba0.5MnO3-γ, J. Phys. Condens. Matter 12 (2000) L155 https://doi.org/10.1088/0953-8984/12/7/103.

[58] Z. Li, K. Wang, M. Cheng, W. Zhou, Study on the electrothermal instability inelectrically exploding aluminum wires in air, Phys. Plasmas 33 (2026) 042103, https://doi.org/10.1063/5.0313237.

[59] A. Ur Rehman, M.I. Arshad, N. Amin, Transport and magnetic properties of Zn0.5Co0.25Cu0.25Ho0.037Fe1.963O4/Graphene nanoplatelets nanocomposites, Ceram. Int. 50 (2024) 55940–55952, https://doi.org/10.1016/j.ceramint.2024.11.004.

[60] A.U. Rehman, S. Sharif, H.H. Hegazy, N. Morley, N. Amin, M. Akhtar, M.I. Arshad, Z. Farooq, Z. Munir, T. Munir, Low dielectric loss, and enhanced magneto-dielectric properties of Cu0.5Cd0.5-xCoxFe2O4 ferrites via Co2+ substitution, Mater. Today Commun. 34 (2023), https://doi.org/10.1016/j.mtcomm.2023.105371.

[61] M.I. Arshad, A. Dastgir, F. Alresheedi, N. Amin, L.D. Tung, M. Amami, N. Thi Kim Thanh, H. Zahid, J. Jacob, S. Ezzine, A.U. Rehman, Electrically and magneto-dielectrically modified La3+ doped Co0.3Li0.1Ca0.5Fe2.1-xLaxO4 spinel ferrites and their potential applications, J. Alloys Compd. 978 (2024) 173015, https://doi.org/10.1016/j.jallcom.2023.173015.

[62] K.L. Lopez Maldonado, P. de la Presa, M.A. de la Rubia, P. Crespo, J. de Frutos, A. Hernando, J.A. Matutes Aquino, J.T. Elizalde Galindo, Effects of grain boundary width and crystallite size on conductivity and magnetic properties of magnetite nanoparticles, J. Nanoparticle Res. 16 (2014) 2482, https://doi.org/10.1007/s11051-014-2482-3.

[63] S.V. Trukhanov, A.V. Trukhanov, S.G. Stepin, H. Szymczak, C.E. Botez, Effect of the size factor on the magnetic properties of manganite La0.50Ba0.50MnO3, Phys. Solid State 50 (2008) 886–893, https://doi.org/10.1134/S1063783408050144.

[64] M.I. Arshad, H. Zahid, M.T. Sajjad, L.D. Tung, N. Amin, N.T.K. Thanh, M. Amami, N. Morley, F. Alresheedi, A. Dastgir, S.M. Siddeeg, M.S. Hasan, Improvements in dielectric, electrical and magnetic contributions in Ca0.5Co0.5CrxFe2-xO4 spinel ferrites by the substitution of Cr3+ ions, Powder Technol. 438 (2024) 119469, https://doi.org/10.1016/j.powtec.2024.119469.

[65] G. Yang, S. Zhou, J. Xiao, H. Zhang, J. Yang, Effect of materials with different permittivity on the sensing depth of open-ended coaxial probes at different frequencies, Rev. Sci. Instrum. 96 (2025) 104711, https://doi.org/10.1063/5.0290728.

[66] M. Hussain, Z. Munir, S.A. Aldulmani, M. Akhtar, M.A. Nabi, S. Knani, H. Mufti, N. Amin, K. Mehmood, M.S. Al Buriahi, S.Z. Ilyas, Enhanced magneto - dielectric and electromagnetic interference shielding properties for medium - frequency applications, J. Mater. Sci. Mater. Electron. 36 (2025) 1–18, https://doi.org/10.1007/s10854-025-16007-z.

[67] N. Ullah Khan, N. Amin, M. Uzair Khalid, M. Amami, M. Ajaz un Nabi, Tailoring the structural, electrical, dielectric, and magnetic properties of graphene nanoplatelets (GNPs)-incorporated Ni0.35Zn0.25Cd0.4Fe2O4 ferrite composites, Mater. Sci. Eng. B 308 (2024) 117580, https://doi.org/10.1016/j.mseb.2024.117580.

[68] R. Samad, M. ud D. Rather, K. Asokan, B. Want, Dielectric and magnetic properties of rare-earth-doped cobalt ferrites and their first-order reversal curve analysis, Appl. Phys. A 125 (2019) 503, https://doi.org/10.1007/s00339-019-2804-5.

[69] G. Yang, S. Zhou, H. Huang, J. Yang, Uncertainty estimation based on the transmission reflection method for measuring the complex permittivity of materials with coaxial airline, Radio Sci. 60 (2025) e2025RS008239, https://doi.org/10.1029/2025RS008239.

[70] R. Zakir, S.S. Iqbal, A.U. Rehman, S. Nosheen, T.S. Ahmad, N. Ehsan, F. Inam, Spectral, electrical, and dielectric characterization of Ce-doped Co-Mg-Cd spinel nano-ferrites synthesized by the sol-gel auto combustion method, Ceram. Int. 47 (2021) 28575–28583, https://doi.org/10.1016/j.ceramint.2021.07.016.

[71] M. Akhtar, A. Ur Rehman, N. Amin, K. Hussain, M. Imran Arshad, Correlation between structural and improved magneto-dielectric behaviour of Li-Mg-Dy ferrite/graphene nanoplatelet composites and their potential applications, J. Magn. Magn Mater. 595 (2024) 171831, https://doi.org/10.1016/j.jmmm.2024.171831.

[72] A. Ur Rehman, G. Abbas, B. Ayoub, N. Amin, M. Ajaz un Nabi, N.A. Morley, M. Akhtar, M. Imran Arshad, M. Uzair Khalid, M. Afzaal, A. Ghuffar, M. Arshad, Impact of Ni2+ on the structural, optical, electrical, and dielectric properties of Cu0.25Co0.25Mg0.5-xNixCe0.03Fe1.97O4 spinel ferrites synthesized via sol-gel auto combustion (SGAC) route, Mater. Sci. Eng. B 291 (2023) 116407, https://doi.org/10.1016/j.mseb.2023.116407.

[73] X. Zhang, Z. Wang, G. Zhou, J. Li, C. Li, C. Lin, X. Xin, Multifunctional metamaterials based on MXene composite aerogels for integrated load-bearing and multiphysics wave attenuation, Composites, Part B Eng. 309 (2026) 113075, https://doi.org/10.1016/j.compositesb.2025.113075.